Journal of Materials Chemistry A

ROYAL SOCIETY OF CHEMISTRY

COMMUNICATION

View Article Online
View Journal | View Issue

Cite this: *J. Mater. Chem. A*, 2022, **10**, 1227

Received 5th October 2021
Accepted 30th November 2021

DOI: 10.1039/d1ta08597b

rsc.li/materials-a

Probing heat generation and release in a 57.5 A h high-energy-density Li-ion pouch cell with a nickel-rich cathode and SiO_x/graphite anode†

Xiaopeng Qi,[ac] Bingxue Liu,[ac] Fengling Yun,[ac] Changhong Wang,[b] Rennian Wang,[ac] Jing Pang,[acd] Haibo Tang,[ac] Wei Quan,[ac] Qiang Zhang,[ac] Man Yang,[ac] Shuaijin Wu,[ac] Jiantao Wang*[acd] and Xueliang Sun*[b]

The electrochemical performance, reliability, and safety of Li-ion cells depend on thermal management. However, the heat generation mechanisms and release characteristics of large-format high-energy-density (HED) Li-ion cells, a prerequisite for an efficient battery thermal management system (TMS), remain unclear. This study clarifies the heat issues of a 57.5 Ah HED (266.9 W h kg^{-1}) Li-ion cell with a promising material couple of nickel-rich cathode and SiO_x/graphite anode. Both reversible entropic heat and irreversible polarization heat at different discharge rates are unraveled. While charge transfer and mass transport dominate the total polarization heat, the contribution from the ohmic effect and surface impedance increases with discharge rates. Polarization heat also increases consistently with lowering SOCs because of the increasing mass transport overpotential. In particular, the abrupt increase of heat generation at a SOC below 25% may be due to the leveraged discharge rate of SiO_x caused by the mismatch of the voltage windows of graphite and SiO_x. Moreover, the isothermal calorimetry study uncovers the significant heat accumulation and delayed heat release effects of large-format cells, which could cause undetectable but dangerous internal temperature rise at high discharge rates. Findings obtained in this study could guide the rational design of HED cells and TMS optimization.

1. Introduction

After powering portable electronic devices for decades, Li-ion batteries (LIBs) are now boosting the worldwide vehicle electrification evolution and starting to penetrate the broad market of massive energy storage systems for renewable energy utilization.[1] To prolong the cruising range of electric vehicles (EVs) and minimize the space occupation of energy stations, intensive research interest has been focused on developing high-energy-density (HED) LIBs.[2] However, in these large-scale energy storage scenarios, some other important performance metrics should be emphasized,[3] including calendar life, energy efficiency, and most importantly safety. Issues in these respects have raised many concerns that are impeding the wide deployment of HED LIBs. Aside from the chemistry and manufacturing quality, cell performances depend significantly on how well the cell temperature can be managed.[4–6] Low temperatures can not only compromise cell outputs because of sluggish charge transfer kinetics and low electrolyte conductivities,[7–9] but can also increase internal shorting risks by lithium plating.[10–12] Comparatively, high temperatures are more detrimental. High temperatures can aggravate side reactions,[13] increase cell impedances,[14] accelerate capacity degradation,[15–17] and in extreme cases can cause separator melting resulting in internal shorting or directly provoke highly-exothermic dangerous chemical reactions inside LIBs.[18]

Heat generation and the resulting temperature variation, however, are inevitable for LIBs, which necessitates the thermal management system (TMS) to maintain the battery temperatures in acceptable ranges.[19–22] The task is challenging for large-format cells frequently used in large-scale HED packs to deduct weights and volumes. Prolonged heat conduction paths and large temperature differences inside large-format cells could render delayed response of the TMS, most of which act based on the feedback of cell surface temperatures. The task of the TMS could be further complicated by the variable and maybe arbitrary battery output demands from EVs and energy stations, which is contrast with the charging process usually performed in much more definite protocols. To achieve timely and efficient battery thermal management, it is necessary to optimize the action and algorithm of heating/cooling systems based on a thorough understanding of the heat generation and release

[a]*China Automotive Battery Research Institute Co., Ltd, No. 11 Xingke Dong Street, Huairou District, Beijing, 101407, China. E-mail: jiantaowang2002@126.com*
[b]*Department of Mechanical and Materials Engineering, University of Western Ontario, 1151 Richmond St, London, Ontario, N6A 3K7, Canada. E-mail: xsun9@uwo.ca*
[c]*GRINM Group Corporation Limited (GRINM Group), No. 2 Xinjiekou Wai Street, Xicheng District, Beijing, 100088, China*
[d]*General Research Institute for Nonferrous Metals, No. 2 Xinjiekou Wai Street, Xicheng District, Beijing, 100088, China*

† Electronic supplementary information (ESI) available. See DOI: 10.1039/d1ta08597b

characteristics of the cell under different output conditions, and not merely relying on the cell surface temperatures.

Among many choices for HED LIBs, the nickel-rich cathode and SiO_x/graphite anode material couple stood out for their commercial viability and has received wide interest across academia to industry. After substantial progress was achieved at the material level in improving the specific capacity and cyclability,[23–27] more and more research interest has been focused on the reliability and safety at the cell level,[28,29] especially after several severe fire and explosion events occurred on some pioneering EV products. The root cause is that the nickel-rich cathode, thinner separators and current collectors preferred in HED cells are generally less high-temperature tolerant and more violent in thermochemical reactions.[30–32] Besides, the large format and high energy density can themselves further aggravate the hazard degree by supporting large-amount and condensed heat release during the cell thermal runaway. A previous study by our group has demonstrated that even a millivolt-level micro short circuit is sufficient to trigger a catastrophic fire in large-format cells with this material couple.[33] The high safety risks and worse consequences narrow the acceptable temperature windows of large-format HED cells and again emphasize the importance of a thorough understanding of the heat generation and release mechanisms. Unfortunately, until now research committed to these issues remain rare.

Herein, this study clarifies the heat issue of a 57.5 Ah Li-ion pouch cell with a high energy density of 266.9 W h kg^{-1} using a $Li[Ni_{0.83}Co_{0.12}Mn_{0.05}]O_2$ NCM cathode and a SiO_x/graphite blended anode. Both reversible entropic heat and irreversible polarization heat at different discharge rates and different SOCs were quantified and analyzed. Electrochemical impedance spectroscopy (EIS) and transient voltage behavior analyses were performed to decompose the polarization heat, and identify the dominant contributing factors and the kinetic limitations. We found that the mismatch of discharge voltage windows of SiO_x and graphite may play a crucial role in increasing the heat generation and cell polarization at low SOCs. More importantly, significant heat accumulation and delayed heat release behavior of large-format HED cells were revealed for the first time by an isothermal calorimetry study.

2. Results and discussion

2.1. The Li-ion cell

The cell has dimensions of 226.6 × 160.2 × 12.2 mm and a weight of 809.1 g, and adopts a $Li[Ni_{0.83}Co_{0.12}Mn_{0.05}]O_2$ NCM cathode with a capacity of 193.9 mA h g^{-1} (Fig. S1†), a SiO_x/graphite blended anode with a capacity of 412 mA h g^{-1}, a ceramic-coated polyethylene (PE) separator with a thickness of 15.3 μm, and an electrolyte of 1 M $LiPF_6$ in EC/DEC/EMC (25 : 50 : 25 by weight). Detailed electrode parameters and an image of the cell are provided in the ESI.† At 1/3C discharge rate and with a voltage window of 4.2–2.8 V, the cell delivered an energy density of 266.9 W h kg^{-1} and a capacity of 57.5 Ah. Cell SOCs were adjusted by discharging fully charged cells (100% SOC) by proportional capacities on the basis of that at 1/3 discharge rate.

2.2. Quantifying the reversible and irreversible heat generation

Newman and his coworkers conducted pioneering research on the general energy balance and heat effects for insertion battery systems.[34–37] The principles proposed in these studies are still being widely used.[38–42] Neglecting the heat related to mixing and phase change,[36] the total heat generation rate for a battery can be described by eqn (1).

$$\dot{Q}_g = I(U - V) - I\left(T\frac{\partial U}{\partial T}\right) \quad (1)$$

where $\dot{Q}_g$ is the heat generation rate and is positive when the system is exothermic, I is the current and is defined as positive for cell discharging, U is the open-circuit voltage (OCV), V is the cell voltage, and T is the temperature.

We first focused on the second term of eqn (1), the entropic heat, which is irreversible and depends on the thermodynamic state of the system. Entropic coefficients at different SOCs, $\partial U/\partial T$ in eqn (1), were measured *via* a potentiometry method reported in our previous work.[43] As can be seen in Fig. 1, the entropic coefficients are positive for SOCs of 100% (0.102 mV k^{-1}), 75% (0.085 mV k^{-1}), and 50% (0.145 mV k^{-1}), indicating endothermic effects for cell discharging and exothermic effects for charging at these SOCs. At 25% and 0% SOCs, the entropic coefficients change to be negative, −0.12 mV k^{-1} and −0.36 mV k^{-1} respectively, suggesting exothermic entropic effects for discharging and endothermic entropic effects for charging. The entropic coefficient for 0% SOC (−0.36 mV k^{-1}) is much larger in absolute value, implying more significant entropic effects. The unsteady voltage at high temperatures is due to cell rebalancing and self-discharge (Fig. S2†). Entropy is in connection with the disorder of a system. At high SOCs, the occupation of

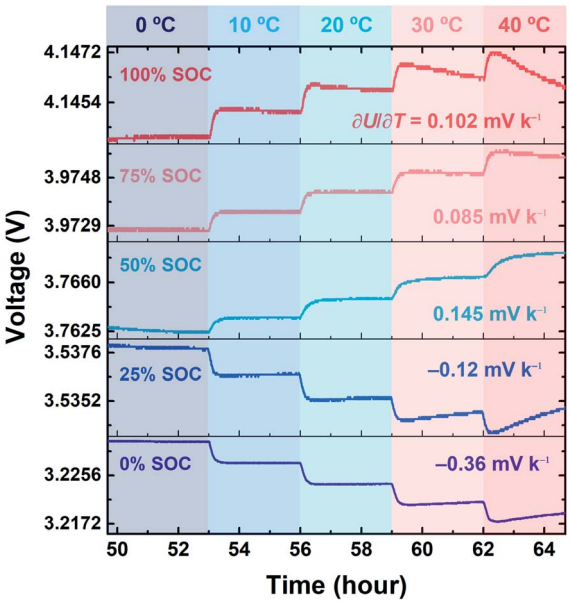

Fig. 1 Responses of the cell voltage to stepped temperature increases and calculated entropic coefficients ($\partial U/\partial T$) of the cell at SOCs of 100%, 75%, 50%, 25%, and 0%.

lithium atoms in both the anode and cathode materials is relatively ordered. Discharging increases the entropy because both Li extraction in the anode and Li insertion in the cathode can occur at many available sites and thus can lead to a more disordered state.[36] Conversely, at lower SOCs, discharging tends to render a full empty state in the anode and a full occupied lattice in the cathode, both of which are more ordered.

We next probed into the first term in eqn (1), the polarization heat, which is irreversible and stems from various overpotentials because of the ohmic effect, charge transfer, and mass transport that are necessary to maintain a required current. To this end, we first estimated the U (denoted as quasi U) by averaging the charge and discharge cell voltages at an ultra-low rate, 0.01C. As can be seen in Fig. 2a, the charge and discharge voltage curves almost overlap with each other at high SOCs, suggesting negligible polarization. They deviate slightly from each other at lower SOCs, indicating that higher overpotentials are required at lower SOCs. Discharge voltage curves at different rates are compared with the quasi U in Fig. 2b. At 1C and 3C rates, the cell capacity decreases by 3.45% and 19.2%, respectively (Fig. 2b), which leads to unused energies of 6.43 W h and 37.1 W h, corresponding to 3% and 17.2% (Fig. 2c) of the total stored energy implied by the quasi U. The area between curve U and curve V represents the energy irreversibly wasted as polarization or overpotential heat, which is 8.4 W h (3.9% of the stored energy) for 1/3C and increases up to 24.6 W h (11.4% of the stored energy) for 3C. To examine the SOC dependence of the heat generation, the overpotentials and equivalent terms for entropic effects selected at certain SOCs (98%, 75%, 50%, 25%, and 0% SOCs) are compared in Fig. 2d. Overpotential at 98% SOC rather than that at 100% SOCs was selected to eliminate the initial transient behavior of cell voltage immediately after discharging. As shown in Fig. 2d, it is obvious that at all discharge rates the overpotentials grow consistently with decreasing SOC and increase sharply below 25% SOC. The heat generation rates were calculated according to eqn (1) and plotted in Fig. 2e–g. As can be seen, the entropic change has significant effects on the total heat generation at the low discharge rate of 1/3C, contributing −28% to 22% to the total heat generation. During cell discharge, the entropic effect reduces the heat generation at higher SOCs but aggravates the heat generation at lower SOCs. It should be noted that the 1/3C discharge rate as used, although is comparatively a low rate in this study, is indeed very representative for electric vehicles and is widely used as a benchmark rate in many power battery testing standards. Higher discharge rates and outputs can also be widely envisioned at scenarios such as EV accelerating and climbing, and electrified aircrafts. At higher discharge rates of 1C and 3C, the overpotential dominates the total heat generation, accounting for more than 85% of the total heat generation.

2.3. Unraveling the irreversible heat generation

The total overpotential consists of partial overpotentials arising from the ohmic effects, heterogeneous charge transfer, and mass transport. Decomposing the total overpotential and quantifying the partial overpotentials are important for

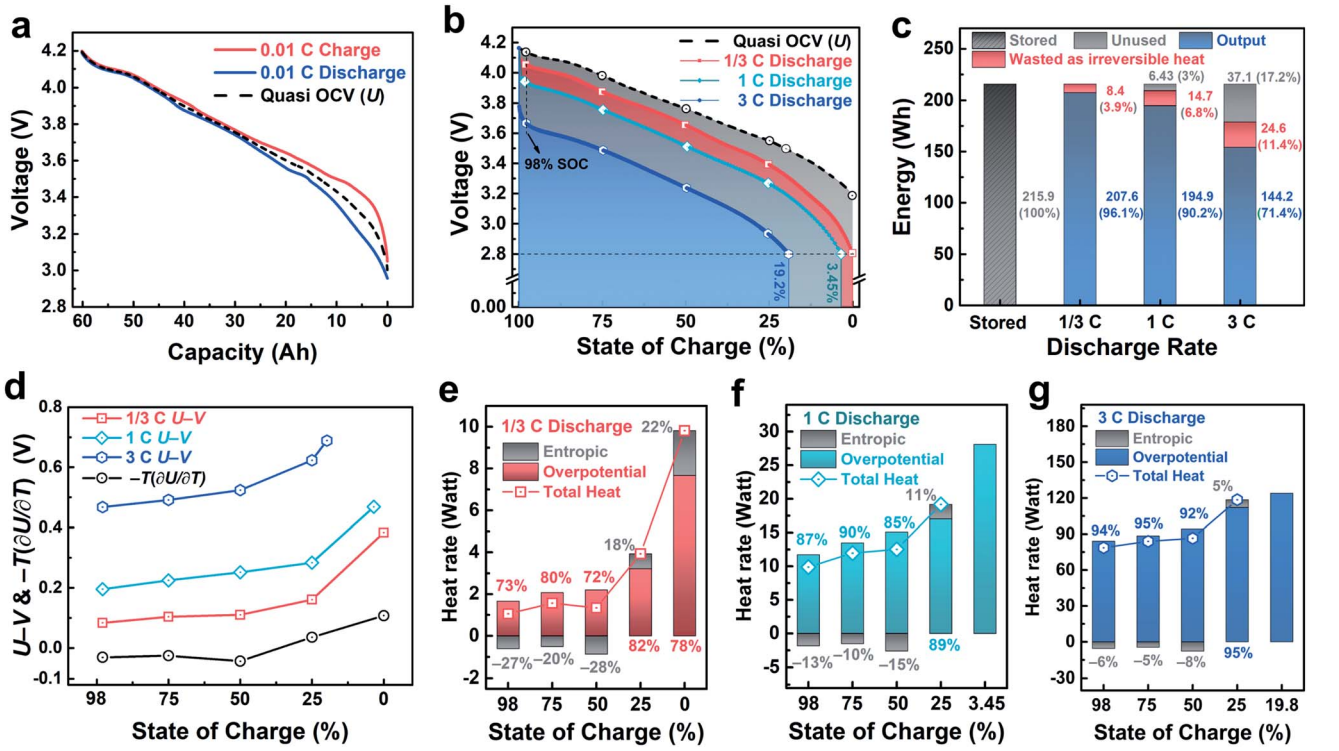

Fig. 2 (a) Voltage curves of the cell during 0.01C charge and discharge and the calculated quasi OCV curve; (b) voltage curves and (c) energy utilization of the cell during 1/3C, 1C, and 3C discharge; (d) overpotentials and entropic-effect equivalents, and (e–g) calculated heat generation rates of the cell during 1/3C, 1C, and 3C discharge.

identifying the dominant factors for the heat generation and, at the same time, the kinetically limiting steps.

We first analyzed the current–overpotential characteristics of the cell. As can be seen in Fig. 3a, the plots at different discharge rates all bend upwards, implying that the currents have not reached the saturation region limited by mass transport but maybe are still being co-controlled by the heterogeneous charge transfer, which is characterized by an exponential-like current-activation overpotential (η_{ac}) relation conforming to the Butler–Volmer equation.[44] EIS tests were further performed to assess the pseudoresistances corresponding to different partial overpotentials. In Fig. 3b, the Nyquist plots exhibit two depressed semicircles in high and medium frequency regions, which can be attributed to impedances from the solid–electrolyte interphase and heterogeneous charge transfer, respectively.[7,45] Using the equivalent circuit model (ECM) in Fig. 3c, the values for R_o (ohmic resistance), R_{SEI} (SEI resistance), and R_{ct} (charge transfer resistance) are fitted out.

Because of the resistive behavior of R_o and R_{SEI}, their contributions to the total overpotential (denoted as η_o and η_{SEI} in Fig. 3d–f) can be calculated and deducted. The residue after the deduction of η_o and η_{SEI} represents the effects of charge transfer (η_{ac}) and mass transport (η_{mt}). Comparing the results shown in Fig. 3d–f reveals that η_{ac} and η_{mt} dominate the total overpotential at all of the SOCs and discharge rates. Their dominating role is more obvious at low discharge rates and especially at low SOCs. For instance, at the 1/3 discharge rate, the collective contribution from η_{ac} and η_{mt} to the total overpotential is 72% (at 98% SOC), 78% (at 75% SOC), 82% (at 50% SOC), 86% (at 25% SOC), and 91% (at 0% SOC), respectively. The contribution from R_o and R_{SEI} gets increasingly important at higher discharge rates. While charge transfer and mass transport properties are almost inherent to the cell material themselves, R_o and R_{SEI} depend significantly on the structure and conducting network in the electrode, and conditions during the initial formation process, and can be improved by design optimization at the cell level.

We further conducted an in-depth examination of the SOC dependence of the resistances shown in Fig. 3c. R_{ct} shows strong SOC dependence and increases significantly at high and low SOCs. This is consistent to previously reported behaviors of the Ni-rich cathode and Si–graphite composite anode.[46–49] R_o and R_{SEI} also show weak SOC dependence, which could be due to the conductivity variation of the active material and SEI as their composition and structure change with the SOC.[50–52] The most notable and in step trend of the resistances is that they all increase significantly from 25% to 0% SOC. R_{ct} increases sharply from 0.41 mΩ at 25% SOC to 1.188 mΩ at 0% SOC. Meanwhile, R_o increases from 0.599 mΩ to 0.752 mΩ and R_{SEI} increases from 0.544 mΩ to 0.89 mΩ. We believe that the in-step increase of all of the resistances from 25% SOC to 0% SOC may have a connection with the SiO_x/graphite blended anode that was used. We noted that graphite and SiO_x hardly overlap with each other in the discharging voltage windows, which is

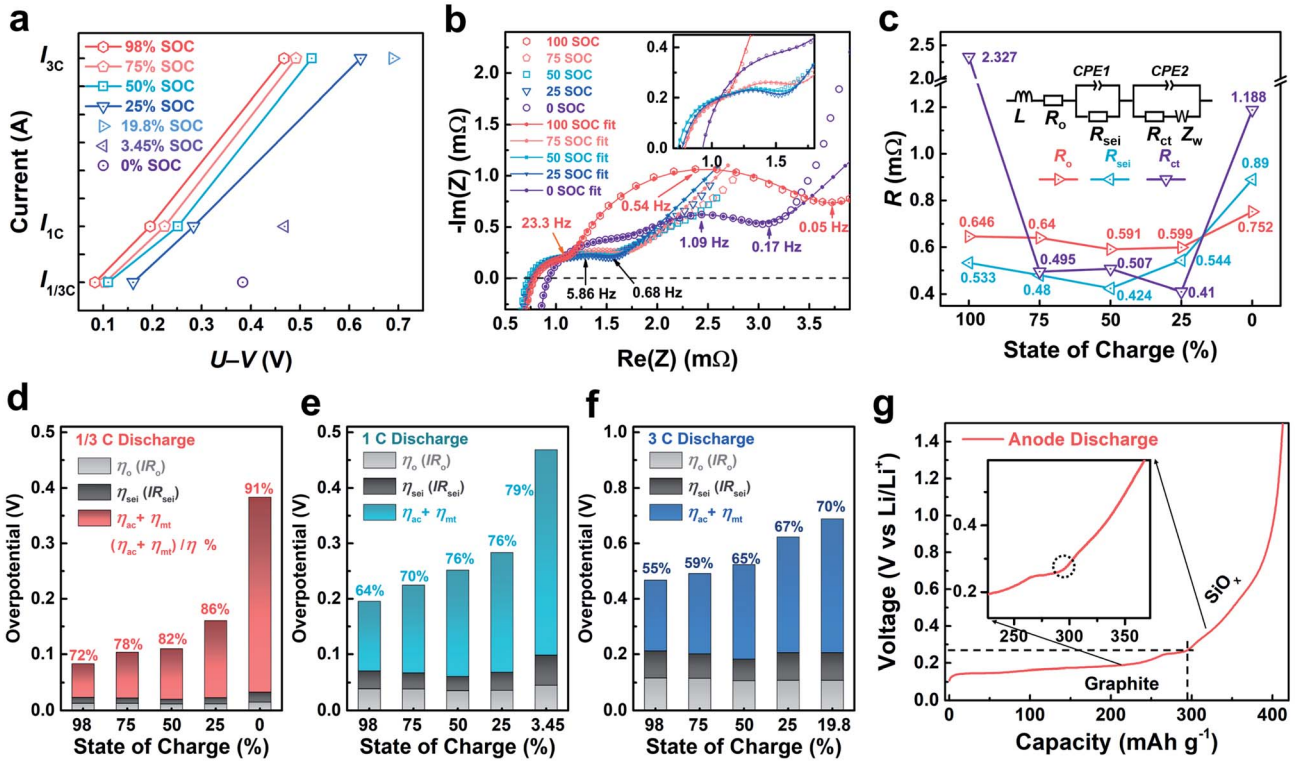

Fig. 3 (a) Current–overpotential plots of the cell; (b) Nyquist plots of the cell under the EIS study and (c) fitted pseudoresistances of the ohmic effect (R_o), SEI (R_{SEI}), and charge transfer (R_{ct}); (d–f) decomposition of the total overpotential; (g) discharge voltage curve of the SiO_x/graphite blended anode at 1/3C.

normally below 0.25 V *vs.* Li/Li^+ for lithiated graphite and above 0.3 V *vs.* Li/Li^+ for lithiated SiO_x.[53–55] This implies that graphite and SiO_x may not discharge simultaneously but may instead discharge successively. As can be seen from the discharge voltage curve of the blended anode shown in Fig. 3g, there is an obvious turning point located at around 0.28 V *vs.* Li/Li^+, below which the voltage curve shows staged features identical to that of graphite.[53] Above 0.28 V, the voltage curve is much more sloped, consistent with that of SiO_x.[55] SiO_x contributes about 27.4% (*ca.* 113 mA h g^{-1}) of the total capacity of the blended anode (412 mA h g^{-1}). In the full cell, because of the N/P ratio (*ca.* 1.15) and narrower real voltage window, the contribution from SiO_x would be further less and should theoretically start below a SOC of *ca.* 24.1%. Since SiO_x weighs only about 10% of the blended anode, the real effective electrode area or electroactive sites would be significantly reduced as discharging is confined to SiO_x at low SOC. This effect may have led to the increase of all of the measured EIS resistances. It also implies that the heat generation would get more concentrated in the location confined to SiO_x. In extreme cases, hot spots could be generated and can be very harmful especially because SEI is generally the most vulnerable components at elevated temperatures.[56] Our previous study evidenced that the onset temperature of SEI decomposition of the SiO_x/graphite blended anode can be as low as 72.03 °C.[33] The successive discharge behavior of the blended anode indicates that the real discharge rates for both graphite and SiO_x would be leveraged. The rate performance burden would be heavier for the component that contributes less capacity, SiO_x in this case. The real discharge rate of SiO_x in this specific anode would at least triple in comparison to the nominal cell discharge rate. This finding emphasizes the importance of matching the voltage windows of the constituents in designing blended electrode materials or further improving their rate performances.

Our remaining task is to separate and assess the contribution from η_{ac} and η_{mt}, requiring quantifying either one of them. We cannot infer η_{ac} directly from R_{ct} measured from the EIS method because R_{ct} is obtained assuming the linear current–activation overpotential relation under small-signal stimulation in the EIS tests. Fortunately, we can take advantage of their differences in response speed to current variation or pulse. η_{ac} generally responds to abrupt current steps relatively fast, although maybe not that fast as the instantaneous response of η_o and η_{SEI}, but η_{mt} shows slow response because developing a concentration gradient is much more time-consuming.[57,58] Their differences in response speed to current steps are consistent with the different characteristic frequencies or time constants in the EIS tests. Following this principle, we performed intermittent cell discharge tests to analyze the transient behaviors of the voltage at SOCs of interest, Fig. 4a. This test appears similar to the current pulse tests for DC resistance measurements,[57,58] but uses actual discharge currents of interest and a much longer timescale to analyze the mass transport effects. Fig. 4b shows the results for the 1/3C discharge rate. The quasi U and ref quasi U were incorporated to correct the SOC effect. When cell voltage becomes tangent to ref quasi U, it implies that the polarization becomes relatively stable and the voltage decrease stems solely from the SOC effect.

The transient voltage curve can be divided into two stages. A prompt voltage drop (ΔV_1) occurs within the first 2 seconds and corresponds to fast response processes including ohmic effects, conduction in the SEI, and charge transfer. By deducting η_o and η_{SEI} from ΔV_1, we extracted the η_{ac}. ΔV_2 accumulates in a timescale of several min and can be attributed mainly to the stabilization of mass transport. It should be noted that η_{ac} is theoretically non-stationary because of the concentration variation of the species adjacent to the heterogeneous reaction interface. Therefore, ΔV_2 may also include the variation of η_{ac} indirectly and this effect can also be ascribed to insufficient mass transport. During discharge from 50% to 25% SOC, the cell voltage never gets tangent to the ref quasi U. It could be because that the marginal effects of discharging (lithium extraction from the anode) on the concentration of lithium in graphite become more and more significant as lithium in graphite become fewer and fewer at low SOCs, as a result η_{ac} and η_{mt} cannot be stabilized. Nevertheless, we still calculated a ΔV_2 for 50% SOC using the data selected at the same time as those in the 100% to 75% SOC tests, *i.e.*, around 5 min after discharge. During discharge from 25% to 0% SOC, the voltage curve experiences a knot at about 3.38 V, which may be indicative of the start of the SiO_x delithiation. The shape of the voltage curve around the knot is also very similar to that of the anode (displayed in the opposite voltage direction) after *ca.* 300 mA h g^{-1} in Fig. 3g.

Comparing η_{ac} and ΔV_2 at different SOCs reveals that the effect of mass transport is more significant under 1/3C discharge conditions, generally occupying more than 50% of the total overpotential. η_{ac} shows similar SOC dependence to that of R_{ct}, featuring extremely high value at 100% SOC and the lowest value at 25% SOC. Overpotential because of mass transport, ΔV_2, grows consistently as SOC gets lowered and increases sharply at 25% SOC. Since none of the lithium diffusion coefficients in graphite and the Ni-rich material exhibit SOC dependence like ΔV_2,[47,59] we believe that the consistent increase of ΔV_2 with lowering SOC may be a result of the decreasing concentration of lithium atoms in the anode and lithium vacancies in the cathode. To maintain a current of a certain magnitude, larger η_{mt} is generally required when the concentration of the electroactive species is lower because both migration and diffusion overpotential tend to increase.[60]

Identical tests and analyses were performed for 1C and 3C discharge rates and the SOC dependencies of η_{ac} and ΔV_2 are the same as those of the 1/3C rate. The consistent increase of the effect of mass transport as the cell discharges may have caused the identical trend of the total overpotential shown in Fig. 3d–f. The voltage curves at 1C discharge rate (Fig. S4†) exhibit similar features to those at 1/3C rate. Notably, the behaviors of the voltage at 3C discharge rate are significantly different. The voltage at 3C rate (Fig. 4c) takes a much shorter period of about 1 min to become stabilized. And the gap between the voltage at 1st second and that at the 2nd second shrink significantly. Compared to those under the 1/3C discharge conditions, η_{ac} under 3C rates increase more than

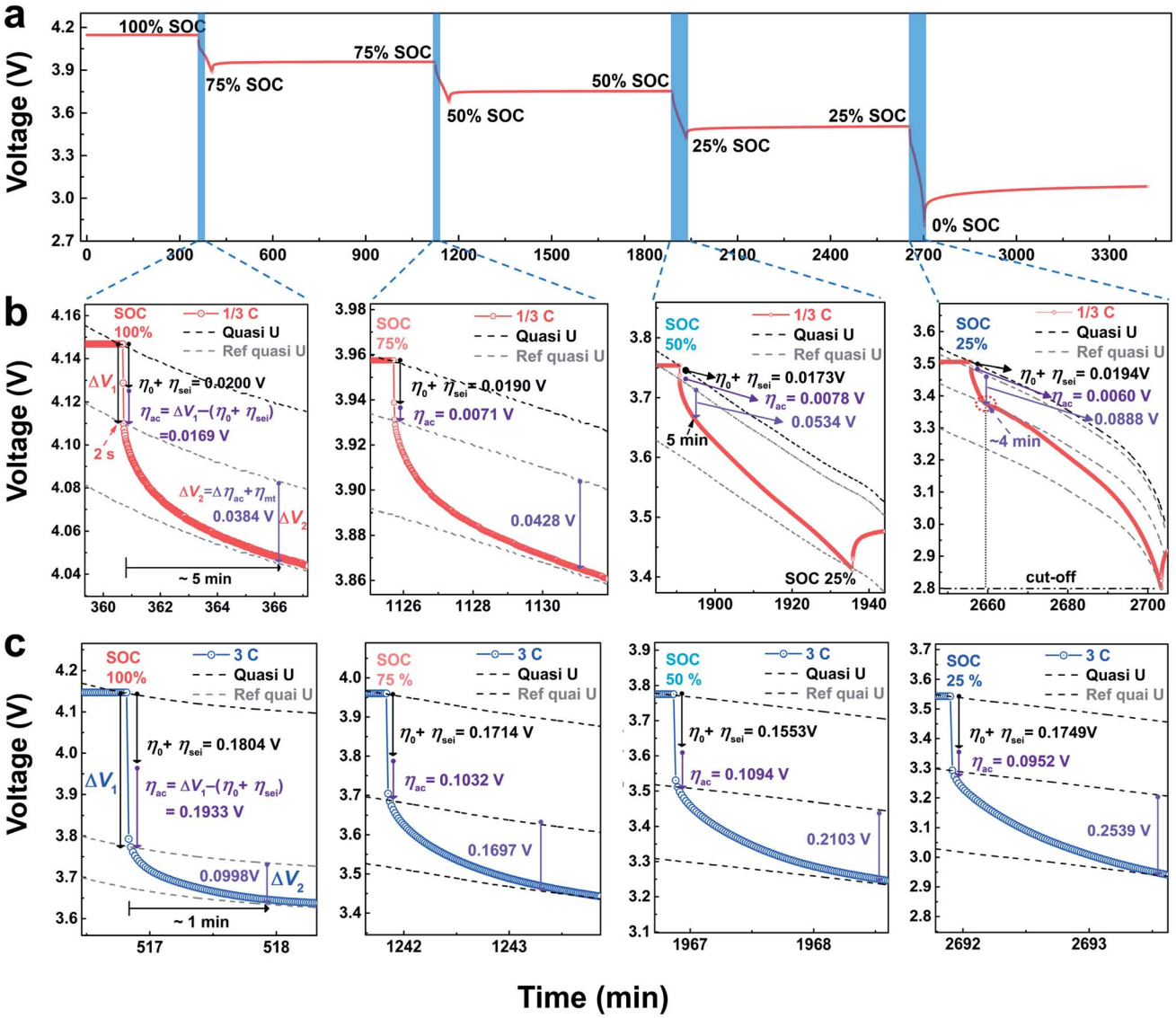

Fig. 4 Transient behaviors and analyses of the discharge voltage of the cell. (a) The full voltage curve at 1/3C discharge rate; selected enlarged section at certain SOCs at (b) 1/3C and (c) 3C discharge rates.

tenfold, which is much more than the increase of the current (eight times). This could be due to the quick and significant depletion/accumulation of active species at the electrode/electrolyte interface at large currents. The drastic increase of η_{ac} at 3C rate could therefore be partially attributed to insufficient mass transport. At the same time, unlike η_{ac}, ΔV_2 at 3C rate generally increases by only 2–4 times, suggesting that at higher discharge rates mass transport imposes more effect on η_{ac} at the reaction interface rather than concentration overpotential in the bulk.

2.4. Unveiling the heat release characteristics

Heat release characteristics of the cell were investigated using an isothermal calorimeter (IC). The principle and the experimental details of the IC test are provided in the ESI. This test well mimics the operating scenario of a TMS with a heating/cooling system attempting to control the cell surface temperature to a preset value or range. The preset cell surface temperature in our test was 25 °C, controlled by the control heater and the cold plates. However, as can be seen from Fig. 5, slight variations of the cell temperatures were found inevitable and became more notable at higher discharge rates. This is due to the imperfect response of the control heater to the abruptly varying heat generation of the cell, which is more obvious at the start and the end of the cell discharge. To better reflect the heat generation rates, the measured heat release rates were adjusted by adding $mC_p(\partial T/\partial t)$, where m is the mass of the cell, $\partial T/\partial t$ is the temperature variation rate, and C_p is the specific heat capacity of the cell, which was measured to be 1.209 J K^{-1} g^{-1} using an accelerating rate calorimeter (ARC), see the ESI.† It should be noted that this adjustment only corrects for the surface temperature variation of the cell and does not capture

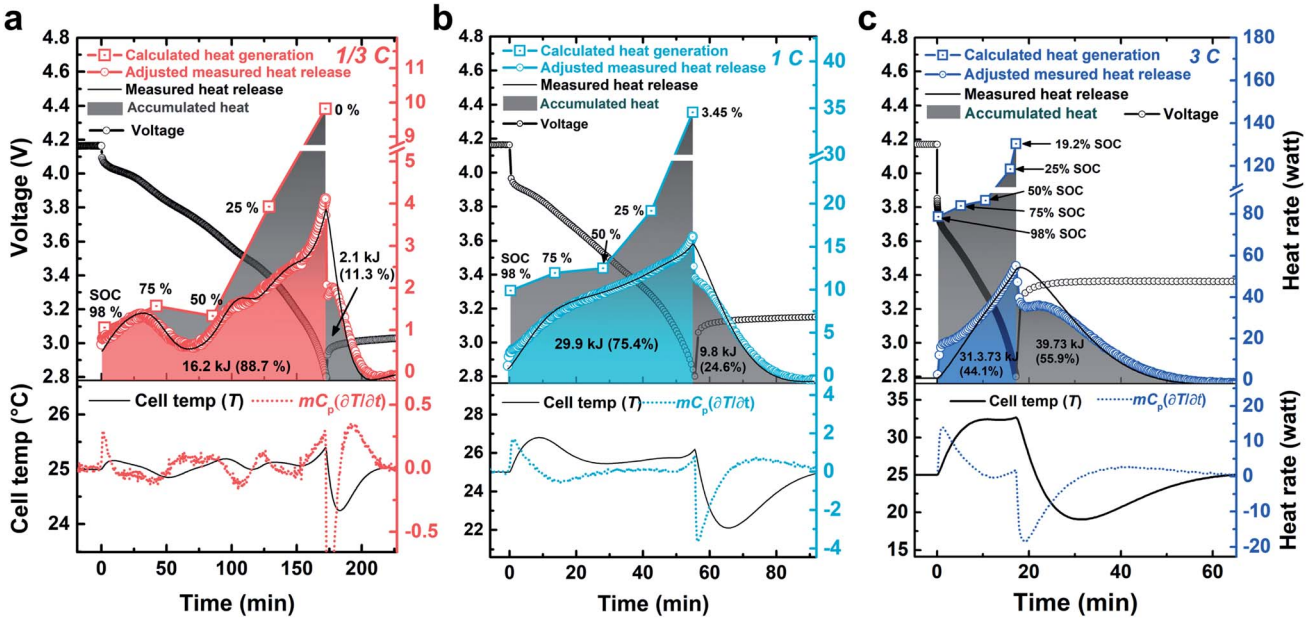

Fig. 5 Heat release rates and temperature variation of the cell at (a) 1/3C, (b) 1C, and (c) 3C discharge rates in the isothermal calorimetry tests. The measured heat release rates were adjusted for the cell surface temperature variation.

the internal cell temperature rise that can be caused by heat accumulation, which is indeed one of the research interests of this study.

Fig. 5a shows the results for the 1/3 discharge condition. As can be seen, the measured heat release rate after adjustment shows similar SOC dependence to that of the calculated heat generation rate but is consistently lower, especially at lower SOCs when cell discharge has persisted for a long period. The temporary fall of the heat generation rate from 75% SOC to 50% SOC because of the increased endothermic entropic effect was also captured. The difference between the heat release rate and the calculated heat generation rate can be explained by internal heat accumulation in the cell, which can cause internal cell temperature rise but cannot be timely captured by the isothermal calorimeter or by the TMS in practice. This is evidenced by the fact that substantial heat release was detected after the cell discharge has stopped. Under the 1/3C discharge conditions, the amount of this residual heat is 2.1 kJ, occupying 11.3% of the total measured heat released. It should be noted that this residue heat may also contain the contribution from the heat of mixing,[36] *i.e.*, relaxation of the concentration gradients, which is, however, usually very small relative to resistance and entropic heat. As can been seen from Fig. 5b and c, as the discharge rate becomes higher, the deviation of heat release rate from the calculated heat rate becomes more significant, suggesting increased heat accumulation. For the 3C rate, the heat release rate reaches 50 watts at the end of the discharge but is still less than half of the theoretical heat generation rate. Meanwhile, the heat release rate curve becomes smoothed, possibly because of the heat sink effect of the cell. The residue heat after the stop of the 3C discharge reaches 39.73 kJ, accounting for 55.9% of the total measured heat released. Assuming uniform temperature within each single laminate and liner temperature gradient along the direction vertical to the laminate stack from the cell center to the broad cell outer surface, the highest temperature at the cell center immediately after the stop of the discharge was estimated to be as high as 98.7 °C. This very high temperature is sufficient to damage the SEI, which can thermally decompose at a temperature as low as 72.03 °C for the SiO_x/graphite composite anode, as was proved in our previous study.[33]

The significant heat accumulation and delayed heat release behaviors of the large-format Li-ion cell suggest that the algorithm of the cooling system and the alarming system of the TMS should not rely merely on the real-time cell surface temperatures. A reliable TMS should take the history outputs, heat generation, and possible heat accumulation effect into consideration, and include the prediction of internal cell temperature rise into its target. Also, deferred shutdown or all-time standby of the TMS would be necessary after the power-off of the EVs. Introducing highly thermally-conductive two-dimensional (2D) materials, such as graphene, to construct more efficient heat conduction networks in the cell and the battery pack may be a possible tactic to alleviate the heat accumulation issue.[61–65]

We also investigated the effects of long cycles on cell heat generation and release characteristics (Fig. S5†). The cell exhibited excellent cycling performances, recording a capacity retention of 92.3% after 363 cycles. After cycling, the entropic effects became more significant at certain SOCs, whereas polarization became alleviated due to better cell kinetics. We speculate that these changes may have connections with the structural evolution and volumetric effects of SiO_x.[55] Expansion, deformation, and pulverization of SiO_x cause capacity loss but at modest levels could also improve electrode electric

conduction and provide smaller particles beneficial to lowering cell polarization. The heat release characteristics of the cycled cell is generally much like that of the fresh cell but with some deviations that are consistent with the variation of the entropic heat.

3. Conclusions

In summary, this study focuses on heat generation and release issues of a 57.5 Ah HED (266.9 W h kg^{-1}) Li-ion cell with a nickel-rich cathode and SiO_x/graphite anode. Apart from the dominance of charge transfer and mass transport for heat generation, we also revealed the significant contribution from the exothermic entropic effect at low discharge rates and the ohmic effect and surface impedance at high discharge rates. Successive discharge behavior of SiO_x and graphite because of the mismatched voltage windows could lead to leveraged rate performances, harmful increased and concentrated heat generation at a SOC below 25%. Significant heat accumulation and delayed heat release behavior of large-format Li-ion cells were uncovered and discussed for the first time, which could induce undetectable but dangerous internal temperature rise at high discharge rates. After 363 cycles, the cell polarization decreased slightly and the entropic effect became more significant at certain SOCs. These findings highlight the drawbacks of many of the current TMS products relying on real-time cell temperature signals, urging optimization of the signal monitoring/collection and algorithms of the TMS to eliminate cell safety risks, and could also shed some light on the design of energy-efficient and high-performance HED Li-ion cells.

Author contributions

Xiaopeng Qi: conceptualization, investigation, formal analysis, writing – original draft. Bingxue Liu: investigation, formal analysis. Fengling Yun: resources, investigation. Changhong Wang: writing – review & editing, formal analysis. Rennian Wang: resources, investigation, project administration. Jing Pang: supervision, conceptualization. Haibo Tang: formal analysis. Wei Quan: resources, investigation. Qiang Zhang: resources, investigation. Man Yang: resources, investigation. Shuaijin Wu: resources, investigation. Jiantao Wang: supervision, conceptualization. Xueliang Sun: supervision, conceptualization.

Conflicts of interest

There are no conflicts to declare.

Acknowledgements

This work was supported by the National Natural Science Foundation of China (Grant No. 21903067, 22005264, and 51604032), Beijing Natural Science Foundation (Grant No. L182023), Guangdong Provincial Science and Technology Commission, Guangdong Key Areas R&D Program (2020B0909030004), and the National Key Research and Development Program of China (Grant No. 2016YFB0100509).

References

1 Z. P. Cano, D. Banham, S. Y. Ye, A. Hintennach, J. Lu, M. Fowler and Z. W. Chen, *Nat. Energy*, 2018, **3**, 279–289.
2 J. W. Choi and D. Aurbach, *Nat. Rev. Mater.*, 2016, **1**, 16013.
3 J. Deng, C. Bae, A. Denlinger and T. Miller, *Joule*, 2020, **4**, 511–515.
4 M.-T. F. Rodrigues, G. Babu, H. Gullapalli, K. Kalaga, F. N. Sayed, K. Kato, J. Joyner and P. M. Ajayan, *Nat. Energy*, 2017, **2**, 17108.
5 N. X. Yang, X. W. Zhang, B. B. Shang and G. J. Li, *J. Power Sources*, 2016, **306**, 733–741.
6 K. C. Chiu, C. H. Lin, S. F. Yeh, Y. H. Lin, C. S. Huang and K. C. Chen, *J. Power Sources*, 2014, **263**, 75–84.
7 S. S. Zhang, K. Xu and T. R. Jow, *Electrochim. Acta*, 2004, **49**, 1057–1061.
8 H.-M. Cho, W.-S. Choi, J.-Y. Go, S.-E. Bae and H.-C. Shin, *J. Power Sources*, 2012, **198**, 273–280.
9 S. S. Zhang, K. Xu and T. R. Jow, *J. Power Sources*, 2003, **115**, 137–140.
10 X. Lai, C. Jin, W. Yi, X. Han, X. Feng, Y. Zheng and M. Ouyang, *Energy Storage Mater.*, 2021, **35**, 470–499.
11 A. Friesen, F. Horsthemke, X. Monnighoff, G. Brunklaus, R. Krafft, M. Borner, T. Risthaus, M. Winter and F. M. Schappacher, *J. Power Sources*, 2016, **334**, 1–11.
12 M. G. Ouyang, Z. Y. Chu, L. G. Lu, J. Q. Li, X. B. Han, X. N. Feng and G. M. Liu, *J. Power Sources*, 2015, **286**, 309–320.
13 F. F. Huang, J. M. Ma, H. Y. Xia, Y. F. Huang, L. Zhao, S. M. Su, F. Y. Kang and Y. B. He, *ACS Appl. Mater. Interfaces*, 2019, **11**, 37357–37364.
14 L. L. Zhang, J. L. Liu, L. Du, P. Fan, X. Xu, Y. L. Ma, P. J. Zuo, B. Qu, G. P. Yin and Q. Fu, *J. Power Sources*, 2021, **496**, 229858.
15 N. Yang, X. Zhang, B. Shang and G. Li, *J. Power Sources*, 2016, **306**, 733–741.
16 P. Ramadass, B. Haran, R. White and B. N. Popov, *J. Power Sources*, 2002, **112**, 606–613.
17 T. M. Bandhauer, S. Garimella and T. F. Fuller, *J. Electrochem. Soc.*, 2011, **158**, R1–R25.
18 Q. Wang, P. Ping, X. Zhao, G. Chu, J. Sun and C. Chen, *J. Power Sources*, 2012, **208**, 210–224.
19 G. Xia, L. Cao and G. Bi, *J. Power Sources*, 2017, **367**, 90–105.
20 W. Wu, S. Wang, W. Wu, K. Chen, S. Hong and Y. Lai, *Energy Convers. Manage.*, 2019, **182**, 262–281.
21 M. L. Hao, J. Li, S. Park, S. Moura and C. Dames, *Nat. Energy*, 2018, **3**, 899–906.
22 Y. Yang, X. P. Huang, Z. Y. Cao and G. Chen, *Nano Energy*, 2016, **22**, 301–309.
23 A. Manthiram, J. C. Knight, S.-T. Myung, S.-M. Oh and Y.-K. Sun, *Adv. Energy Mater.*, 2016, **6**, 1501010.
24 W. Liu, P. Oh, X. Liu, M.-J. Lee, W. Cho, S. Chae, Y. Kim and J. Cho, *Angew. Chem., Int. Ed.*, 2015, **54**, 4440–4457.

25 S.-T. Myung, F. Maglia, K.-J. Park, C. S. Yoon, P. Lamp, S.-J. Kim and Y.-K. Sun, *ACS Energy Lett.*, 2017, **2**, 196–223.
26 J. R. Szczech and S. Jin, *Energy Environ. Sci.*, 2011, **4**, 56–72.
27 X. Su, Q. Wu, J. Li, X. Xiao, A. Lott, W. Lu, B. W. Sheldon and J. Wu, *Adv. Energy Mater.*, 2014, **4**, 1300882.
28 X. N. Feng, D. S. Ren, X. M. He and M. G. Ouyang, *Joule*, 2020, **4**, 743–770.
29 X. Feng, M. Ouyang, X. Liu, L. Lu, Y. Xia and X. He, *Energy Storage Mater.*, 2018, **10**, 246–267.
30 W. D. Li, E. M. Erickson and A. Manthiram, *Nat. Energy*, 2020, **5**, 26–34.
31 H. Lee, M. Yanilmaz, O. Toprakci, K. Fu and X. W. Zhang, *Energy Environ. Sci.*, 2014, **7**, 3857–3886.
32 P. Arora and Z. M. Zhang, *Chem. Rev.*, 2004, **104**, 4419–4462.
33 X. Qi, B. Liu, J. Pang, F. Yun, R. Wang, Y. Cui, C. Wang, K. Doyle-Davis, C. Xing, S. Fang, W. Quan, B. Li, Q. Zhang, S. Wu, S. Liu, J. Wang and X. Sun, *Nano Energy*, 2021, **84**, 105908.
34 D. Bernardi, E. Pawlikowski and J. Newman, *J. Electrochem. Soc.*, 1985, **132**, 5–12.
35 L. Rao and J. Newman, *J. Electrochem. Soc.*, 1997, **144**, 2697–2704.
36 K. E. Thomas and J. Newman, *J. Power Sources*, 2003, **119**, 844–849.
37 K. E. Thomas and J. Newman, *J. Electrochem. Soc.*, 2003, **150**, A176–A192.
38 S. Panchal, I. Dincer, M. Agelin-Chaab, R. Fraser and M. Fowler, *Int. J. Heat Mass Transfer*, 2016, **101**, 1093–1102.
39 K. Onda, H. Kameyama, T. Hanamoto and K. Ito, *J. Electrochem. Soc.*, 2003, **150**, A285–A291.
40 B. Manikandan, C. Yap and P. Balaya, *J. Electrochem. Soc.*, 2017, **164**, A2794–A2800.
41 S. J. Drake, M. Martin, D. A. Wetz, J. K. Ostanek, S. P. Miller, J. M. Heinzel and A. Jain, *J. Power Sources*, 2015, **285**, 266–273.
42 Y. Bai, L. M. Li, Y. Li, G. H. Chen, H. C. Zhao, Z. H. Wang, C. Wu, H. Y. Ma, X. Q. Wang, H. Y. Cui and J. Zhou, *J. Energy Chem.*, 2019, **29**, 95–102.
43 F.-L. Yun, W.-R. Jin, L. Tang, W. Li, J. Pang and S.-G. Lu, *J. Electrochem. Soc.*, 2016, **163**, A639–A643.
44 A. J. Bard and L. R. Faulkner, *Electrochemical Methods: Fundamentals and Applications*, John Wiley & Sons, Inc, 2nd edn, 2001.
45 Y. Zhang and C.-Y. Wang, *J. Electrochem. Soc.*, 2009, **156**, A527.
46 C. Y. Hong, Q. Y. Leng, J. P. Zhu, S. Y. Zheng, H. J. He, Y. X. Li, R. Liu, J. J. Wan and Y. Yang, *J. Mater. Chem. A*, 2020, **8**, 8540–8547.
47 C. Zhang, J. Wan, Y. Li, S. Zheng, K. Zhou, D. Wang, D. Wang, C. Hong, Z. Gong and Y. Yang, *J. Mater. Chem. A*, 2020, **8**, 6893–6901.
48 M. D. Levi, K. Gamolsky, D. Aurbach, U. Heider and R. Oesten, *Electrochim. Acta*, 2000, **45**, 1781–1789.
49 X. M. Li, A. M. Colclasure, D. P. Finegan, D. S. Ren, Y. Shi, X. N. Feng, L. Cao, Y. Yang and K. Smith, *Electrochim. Acta*, 2019, **297**, 1109–1120.
50 M. Park, X. Zhang, M. Chung, G. B. Less and A. M. Sastry, *J. Power Sources*, 2010, **195**, 7904–7929.
51 A. Funabiki, M. Inaba, Z. Ogumi, S. Yuasa, J. Otsuji and A. Tasaka, *J. Electrochem. Soc.*, 1998, **145**, 172–178.
52 C. K. Chan, R. Ruffo, S. S. Hong and Y. Cui, *J. Power Sources*, 2009, **189**, 1132–1140.
53 T. Ohzuku, Y. Iwakoshi and K. Sawai, *J. Electrochem. Soc.*, 1993, **140**, 2490–2498.
54 J. Yang, Y. Takeda, N. Imanishi, C. Capiglia, J. Y. Xie and O. Yamamoto, *Solid State Ionics*, 2002, **152**, 125–129.
55 T. Chen, J. Wu, Q. L. Zhang and X. Su, *J. Power Sources*, 2017, **363**, 126–144.
56 X. Feng, M. Fang, X. He, M. Ouyang, L. Lu, H. Wang and M. Zhang, *J. Power Sources*, 2014, **255**, 294–301.
57 W. Waag, S. Käbitz and D. U. Sauer, *Appl. Energy*, 2013, **102**, 885–897.
58 A. Barai, K. Uddin, W. D. Widanage, A. McGordon and P. Jennings, *Sci. Rep.*, 2018, **8**, 21.
59 M. D. Levi and D. Aurbach, *J. Phys. Chem. B*, 1997, **101**, 4641–4647.
60 J. Newman and K. E. Thomas-Alyea, *Electrochemical Systems*, John Wiley & Sons, Inc, Hoboken, New Jersey, 3rd edn, 2004.
61 P. Goli, S. Legedza, A. Dhar, R. Salgado, J. Renteria and A. A. Balandin, *J. Power Sources*, 2014, **248**, 37–43.
62 A. Hussain, I. H. Abidi, C. Y. Tso, K. C. Chan, Z. T. Luo and C. Y. H. Chao, *Int. J. Therm. Sci.*, 2018, **124**, 23–35.
63 B. Mortazavi, H. L. Yang, F. Mohebbi, G. Cuniberti and T. Rabczuk, *Appl. Energy*, 2017, **202**, 323–334.
64 D. Q. Zou, X. F. Ma, X. S. Liu, P. J. Zheng and Y. P. Hu, *Int. J. Heat Mass Transfer*, 2018, **120**, 33–41.
65 B. Zhao, X. Z. Fu, R. Sun and C. P. Wong, *Sustainable Energy Fuels*, 2017, **1**, 2145–2154.